Proceedings of the ASME 2014 Dynamic Systems and Control Conference
DSCC2014
October 22-24, 2014, San Antonio, TX, USA

DSCC2014-6321

PARAMETERIZATION AND VALIDATION OF A DISTRIBUTED COUPLED ELECTRO-THERMAL MODEL FOR PRISMATIC CELLS

Nassim A. Samad
Jason B. Siegel
Anna G. Stefanopoulou
Department of Mechanical Engineering
University of Michigan
Ann Arbor, MI 48019
Email: nassimab@umich.edu

ABSTRACT

The temperature distribution in a prismatic Li-ion battery cell can be described using a spatially distributed equivalent circuit electrical model coupled to a 3D thermal model. The model represents a middle ground between simple one or two state models (generally used for cylindrical cells) and complex finite element models. A lumped parameter approach for the thermal properties of the lithium-ion jelly roll is used. The battery is divided into $(m \times n)$ nodes in 2-dimensions, and each node is represented by an equivalent circuit and 3 temperatures in the through plane direction to capture the electrical and thermal dynamics respectively. The thermal model is coupled to the electrical through heat generation. The parameters of the equivalent circuit electrical model are temperature and state of charge dependent. Parameterization of the distributed resistances in the equivalent circuit model is demonstrated using lumped parameter measurements, and are a function of local temperature. The model is parameterized and validated with data collected from a 3-cell fixture which replicates pack cooling conditions. Pulsing current experiments are used for validation over a wide range of operating conditions (ambient temperature, state of charge, current amplitude and pulse width). The model is shown to match experimental results with good accuracy.

1 INTRODUCTION

Growing use and acceptance of Li-ion batteries in automotive and high-power applications is the result of advances in battery cost and overall system safety. Accurate battery models are necessary to define the safe operating limits, both thermal and electro-chemical, of the battery cell without sacrificing performance due to overly conservative bounds. Battery temperature must be regulated under high power operation due to internal heating of the cell. If the temperature rises above the breakdown temperature of the electrolyte or solid electrolyte interface, thermal runaway could occur [1]. Researchers have focused on analyzing and understanding the behavior of lithium-ion cells as a means to overcome these obstacles. Bernardi et al. [2] proposed a general energy balance for batteries to predict temperature. Successive researchers have attempted different approaches to modeling the thermal and electrical behavior of lithium-ion batteries. Physics based models [3–5] which solve the governing equations due to lithium-ion transport in the cell can predict microscopic level behavior and performance, but require large computational power to solve the differential equations. Other models, which are more adequate for control oriented purposes, such as the battery management system (BMS) of a vehicle, employ electrical circuit elements [6–15] to model the physical responses of the battery. These models are relatively easy to parameterize and can yield sufficiently accurate results that justify their use in battery management systems.

Cylindrical cells have been studied thoroughly. Models that

predict internal cell temperatures can be used to regulate cell temperature. Gao at al. [11] formulated a single RC equivalent circuit model with temperature and state of discharge (SOD) dependent open circuit voltage (OCV), coupled with a "bulk" thermal model that characterizes the whole battery as one uniform temperature. Perez et al. [12] expanded on Gao's model to include a two state thermal model (surface and core) coupled with a double RC equivalent circuit model with temperature and state of charge dependent parameters. Smith et al. [14] used finite volume methods to model the temperature distributions along with a representative equivalent circuit model.

Prismatic cells can be packaged more efficiently than cylindrical cells. However, they are harder to model because tabbing configurations impact spatial temperature profiles. Many techniques were proposed in literature for modeling the thermal behavior of prismatic cells [7, 13, 15–20]. Wang at al. [16] considered different thermal models and studied the computational efficiency and accuracy of these models. Inui et al. [17] considered the effect of the cross-sectional area of a prismatic battery on the temperature distributions within that battery. Gualous et al. [18] developed a new thermal parameter estimation tool using a first order Cauer thermal model, and investigated the behavior of a battery under abuse conditions. Other more recent models have presented coupled electro-thermal models that can predict temperature distributions in a prismatic cell [7, 13, 19]. In particular, coupled electro-thermal models with distributed equivalent circuits [7, 13] have been able to capture the local dynamics of prismatic cells and observe the local variations in temperature, current and SOC.

In what follows, we investigate a new model that couples the electrical and thermal behavior of a prismatic cell which includes local current, states of charge and temperature distributions. This model combines aspects of complex finite element models with simple one or two state models. It couples a 3-D thermal network with surface nodes and interior (core) nodes that lump the average properties of the jelly roll inside the battery, with an electrical model of distributed double RC equivalent circuits at each interior node. The distributed nodal mesh allows for validation with new thin film sensors with 0.5^oC accuracy that are mounted on the surface of the cell to capture spatial temperature variations in replicated pack conditions. Unlike simple one and two state models, this distributed temperature model is needed to understand the spatial temperature distribution and predict hot spots induced by airflow, while maintaining a fast computational approach. It also addresses the issue of sensor placement on the surface of the cell. Model results show good agreement with experimental data over a wide range of temperatures, SOCs and C-rates.

2 Coupled Electro-thermal Model

The model presented here couples a 3-D thermal model with a distributed equivalent circuit model. The electrical model generates output of terminal voltage, SOC and heat generation. The heat generation feeds into the thermal model to determine the temperature distributions which then feed into the electrical model to determine the electrical properties which are a function of temperature.

2.1 Experimental Conditions

A Lithium-Nickel-Manganese-Cobalt-Oxide battery was used in our experiments. The cell is $120mm \times 85mm \times 12.7mm$ and has a nominal 5Ah capacity. The battery is instrumented with an array of RTD (resistance temperature detector) sensors on either side and an NTC (negative temperature coefficient) thermistor close to the battery tab as shown in Fig. 1. In total there are 36 RTDs on either side of the battery to measure spatial temperature distributions. These RTD sensors are mounted on the dimples of a spacer that allows for airflow between the cells while maintaining compression of the fixture. The battery is clamped between two other similar batteries and placed in a Cincinnati Sub-Zero ZPHS16-3.5-SCT/AC environmental chamber for ambient temperature control. The fixture has a fan connection to allow for flow control. This setup was designed to replicate the conditions present in an actual vehicle, where the cells are stacked in an array. The RTDs allow for measurements of temperature while the cell is operating under conditions similar to that in the vehicle.

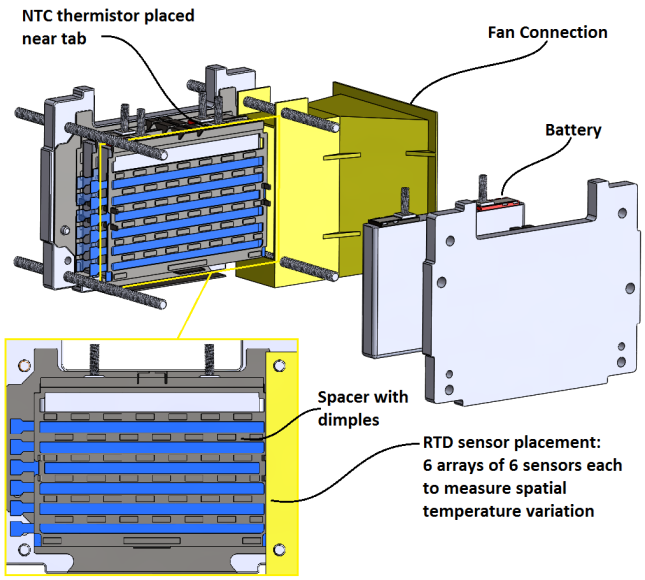

FIGURE 1. EXPLODED VIEW OF FIXTURE USED IN EXPERIMENTS

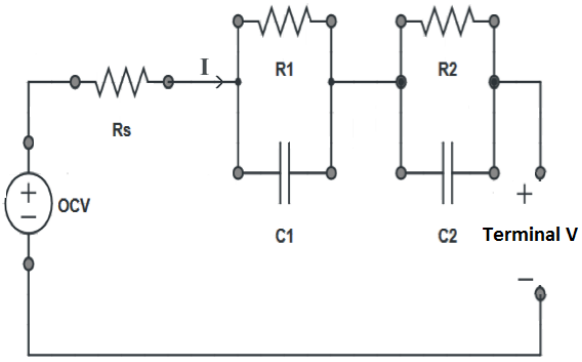

FIGURE 2. DOUBLE RC MODEL REPRESENTING THE CELL

2.2 Detailed Electrical Model

In order to simulate the SOC and current variation at different spatial locations of the battery, a double RC model is implemented at each interior thermal node. Figure 2 shows a schematic of the equivalent circuit model at each node. The series resistance R_s represents the internal resistance of the cell, which accounts for ohmic losses. The pairs (R_1, C_1) and (R_2, C_2) represent the resistances and capacitances that account for lithium diffusion in the solid and electrolyte. The open circuit voltage, which represents the voltage of the cell with no applied current, is a function of state of charge.

The electrical model assumes that the current collectors are infinitely conductive and does not account for tabbing. At each $(n \times m)$ 2-D spatial node, a double RC equivalent circuit model is used to determine the local through-plane current density. Hence:

$$I_{total} = I_1 + I_2 + ... + I_{nm} \tag{1}$$

and for each node, Kirchhoff's voltage law applies so that at node i, we have:

$$OCV_i - I_i R_{s,i} - V_{1,i} - V_{2,i} = V_{terminal} \tag{2}$$

So for an input I_{total}, since $V_{1,i}, V_{2,i}$, and OCV_i are states in this model, we can solve the following equation to get the local distributions of I:

$$\begin{bmatrix} 1 & 1 & ... & 1 & 0 \\ R_{s,1} & 0 & ... & 0 & 1 \\ 0 & R_{s,2} & ... & 0 & 1 \\ . & . & . & . & . \\ 0 & 0 & ... & R_{s,nm} & 1 \end{bmatrix} \begin{bmatrix} I_1 \\ I_2 \\ I_3 \\ . \\ V_{terminal} \end{bmatrix} = \begin{bmatrix} I_{total} \\ OCV_1 - V_{1,1} - V_{2,1} \\ OCV_2 - V_{1,2} - V_{2,2} \\ . \\ OCV_{nm} - V_{1,nm} - V_{2,nm} \end{bmatrix}$$

The state equations representing each node are:

$$\begin{bmatrix} \dot{V}_{1,i} \\ \dot{V}_{2,i} \\ \dot{z}_i \end{bmatrix} = \begin{bmatrix} -\frac{1}{R_{1,i}C_{1,i}} & 0 & 0 \\ 0 & -\frac{1}{R_{2,i}C_{2,i}} & 0 \\ 0 & 0 & 0 \end{bmatrix} \begin{bmatrix} V_{1,i} \\ V_{2,i} \\ z_i \end{bmatrix} + \begin{bmatrix} \frac{1}{C_{1,i}} \\ \frac{1}{C_{2,i}} \\ -\frac{1}{Q} \end{bmatrix} \begin{bmatrix} I_{1,i} \end{bmatrix}$$

where Q is the nominal capacity of the cell and z is the state of charge of the cell.

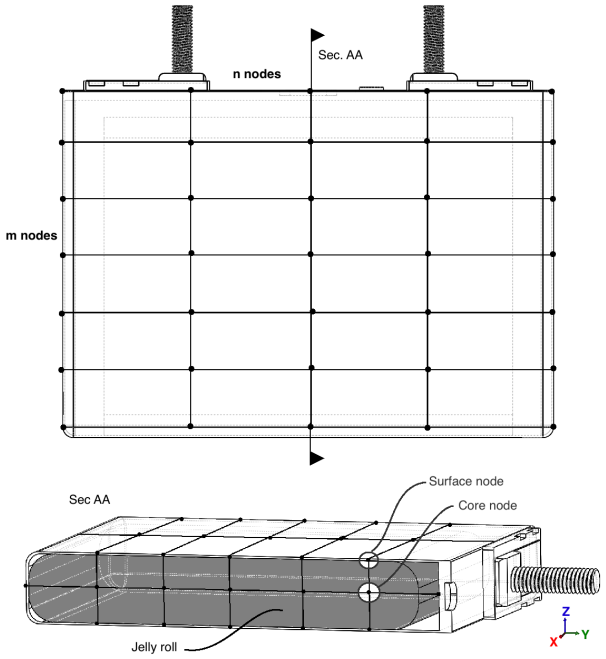

FIGURE 3. 3 LAYERED $N \times M$ MESH FOR THERMAL MODEL

2.3 Detailed Thermal Model

A 3-D thermal model is also implemented where a 3 layered-user defined $n \times m$ mesh is introduced as shown in Fig. 3. The middle layer represents the core nodes, while the upper and lower

layers represent the nodes at the surface of the battery. The thermal properties of aluminum are used for the surface nodes corresponding to the casing with a measured thickness of 0.6mm. Air gaps exist between the jelly roll and the aluminum casing and are also modeled using air thermal properties. This simplified model, where the core nodes represent the average properties of the jelly roll, is shown to be sufficiently accurate but much faster than a detailed model [16]. Heat generation occurs at the core nodes, and surface convection occurs at the surface nodes. Conduction in the cell is assumed to be anisotropic as the thermal conductivities across the x-y plane and z-axis are an order of magnitude different as reported in [20, 21]. Moreover, since the aluminum shell is relatively thin compared to the jell roll, the heat conduction from the interior nodes to the surface nodes is dictated by the thermal conductivity of the jelly roll in the z-axis.

Heat transfer in each node in the cell is governed by the general heat equation:

$$\rho c V \frac{dT}{dt} = \dot{Q}_{gen} + \dot{Q}_{in} - \dot{Q}_{out} \tag{3}$$

where ρ is the density of the the unit volume, c is the specific heat capacity, and V the volume of that unit. $\dot{Q}_{gen}$ represents the heat generation in the unit volume, which would be:

$$\dot{Q}_{gen} = I^2 R_s + \frac{V_1^2}{R_1} + \frac{V_2^2}{R_2} + IT\frac{dU}{dT} \tag{4}$$

where the first 3 terms of Eqn. 4 represent ohmic heat losses, and the last term represents the entropic heat generation. $\dot{Q}_{in} - \dot{Q}_{out}$ represents the net heat conduction and/or surface convection into the unit volume, depending on the location of the node (i.e. core or surface). For an interior node i, the net heat flow is:

$$\begin{aligned} \dot{Q}_{in} - \dot{Q}_{out} = &\sum \frac{K_{inplane} A_{in}}{L_{in}} (T_{srd-core,i} - T_i) \\ &+ \sum \frac{K_{crossplane} A_{cross}}{L_{cross}} (T_{surface} - T_i) \end{aligned} \tag{5}$$

where $K_{inplane}$ is the thermal conductivity in the $xy-plane$, while $K_{crossplane}$ is the thermal conductivity along the $z-axis$ as shown in Fig. 3. A_{cross}, L_{cross}, and A_{in}, L_{in} are the corresponding areas and lengths between neighboring volumes, and $T_{srd-core}$ is the temperature of the surrounding core nodes. For a surface node, the net heat flow is:

$$\begin{aligned} \dot{Q}_{in} - \dot{Q}_{out} = &\sum \frac{K_{Al} A_{in}}{L_{in}} (T_{srd-surface,i} - T_i) \\ &+ \sum \frac{K_{crossplane} A_{cross}}{L_{cross}} (T_{core,i} - T_i) \\ &+ h_{surface} A_{surface} (T_{amb} - T_i) \end{aligned} \tag{6}$$

where K_{Al} is the thermal conductivity of aluminum, $h_{surface}$ is the surface convection over the surface of the battery, and $T_{srd-surface}$ is the temperature of surrounding surface nodes. Note that radiative heat transfer could contribute up to 63% of the overall heat transfer out of the cell [16], but in this experiment, the cells are enclosed in a fixture as shown in Fig. 1, which limits the radiative heat transfer considerably. Thus $h_{surface}$ would be representative of the heat transfer coefficient over the surface of the battery. Finally for those nodes that are on the edges (not the surface), another heat transfer coefficient h_{edge} is considered since the conditions on the surface and the edges of the battery are different. Note that $h_{surface}$ and h_{edge} are a function of flow conditions, and are constant for a given flow condition.

2.4 Electrical Parameterization

The distributed model requires that electrical parameters be identified at each node of the jelly roll. To achieve this, one double RC model was assumed to represent the entire jelly roll. Electrical parameterization was done under controlled conditions at different temperatures and SOCs. Figure 4 shows the current profile used for parameterization. The battery was charged to 100% SOC and allowed to relax, and then a series of pulses were performed at each SOC. The pulses consisted of a (5A, -5A, 15A, -15A) pulses of 10 sec duration with 200 sec rest after the (5A, -5A) pulses and 300 sec rest after the (15A, -15A) pulses. This parameterization was done at T =45, 35, 25, 15, 5, and -5^{o}C. A fine parameterization was done at the higher and lower SOCs since a bigger change in the electrical parameters is expected at those SOCs.

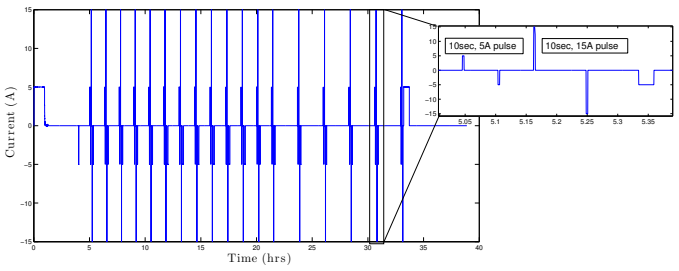

FIGURE 4. CURRENT PROFILE USED FOR ELECTRICAL PARAMETERIZATION

Figure 5 shows the voltage fit on the relaxation data after a CC (constant current) discharge pulse, and the error on the fit for 3 models: single, double and triple RC models, at 3 different SOC (30%, 50%, and 70%). The double and triple RC models provide a better fit to the data than the single RC model since the error on the voltage fit is smaller. The double RC model is

chosen over the triple RC model because it is simpler and computationally faster. The resulting electrical parameters are also plotted in Fig. 6. As expected the electrical resistances decrease with increasing temperature and increase at lower SOCs. The behavior of R_s as a function of temperature seems to follow an Arrhenius relationship, where the resistance increases exponentially as a function of decreasing temperature.

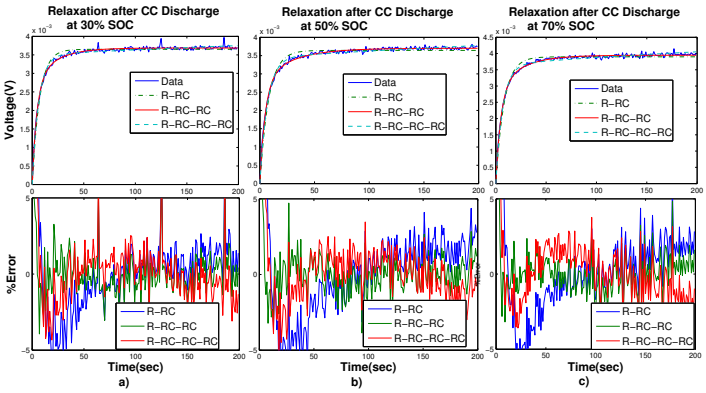

FIGURE 5. VOLTAGE FIT AND ERROR FOR SINGLE, DOUBLE AND TRIPLE RC MODELS AT a) 30% SOC b) 50% SOC c) 70% SOC

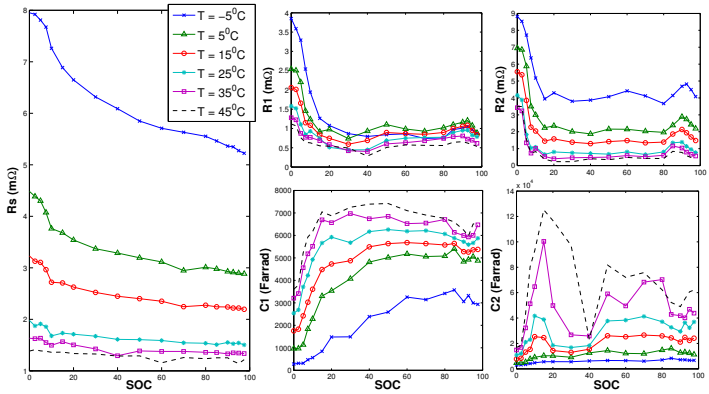

FIGURE 6. ELECTRICAL PARAMETERS R_s, R_1, C_1, R_2, and C_2 AS A FUNCTION OF SOC AND TEMPERATURE

Fig. 7 shows the time constants for the double RC pairs (R_1, C_1) and (R_2, C_2) at different temperatures. As expected, the electrical response of the battery has 2 time constants that are an order of magnitude different. The larger time constant also shows that the battery relaxes slower at lower and higher SOCs.

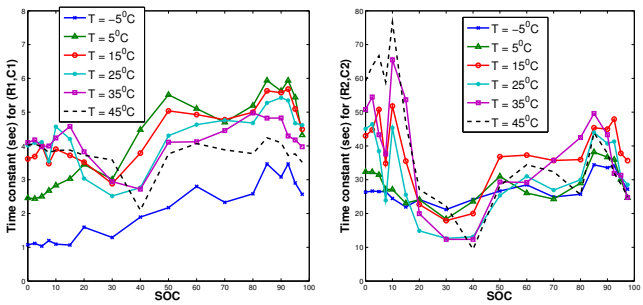

FIGURE 7. TIME CONSTANTS FOR BOTH RC PAIRS AT DIFFERENT TEMPERATURES

Finally, in order to characterize the entropy of the battery, a voltage relaxation method was used [22]. The method consists of charging or discharging the battery to a certain SOC, letting it relax and then changing the temperature to measure the voltage change. The value of $\frac{dU}{dT}$ is the slope of the OCV as a function of temperature at that SOC. Figure 8 shows the slope $\frac{dU}{dT}$ at different SOCs. Since for a lithium cobalt oxide cell, entropy change is a strong function of SOC and not temperature [17], entropy change for the lithium-ion cell considered in this paper is assumed to be a function of SOC only. Thus, this experiment was performed at 25^oC and the results are considered representative of the range of temperatures in our experiments. Depending on the sign of current and $\frac{dU}{dT}$, the value of $IT\frac{dU}{dT}$ could be positive or negative implying an exothermic or endothermic reaction respectively. This effect would be observable at low charge or discharge rates where the ohmic heat generation is small compared to the entropic heat generation. At values of SOC between 45% SOC and 80% SOC, the entropy coefficient is positive, but it is negative beyond these points.

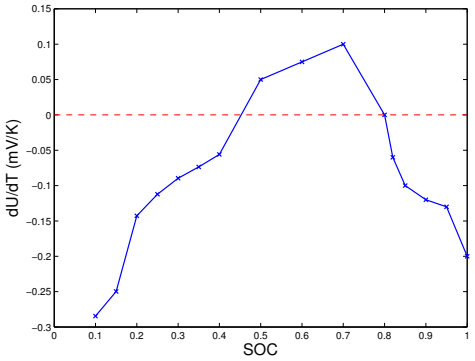

FIGURE 8. ENTROPY SLOPE $\frac{dU}{dT}$ AS A FUNCTION OF SOC AS MEASURED DURING DISCHARGE AT 25^oC

To expand this model into a distributed double RC model, the electrical resistances (R_s, R_1, R_2) are distributed in parallel (i.e. $\frac{1}{R_s} = \sum_{i=1}^{nm} \frac{1}{R_{s,i}}$) among the core nodes, and accordingly, to maintain the time constant, the capacitances (C_1, C_2) are distributed in series (i.e. $C_1 = \sum_{i=1}^{nm} C_{1,i}$). This agrees with the assumption in section 2.2 that terminal voltage across all core nodes is the same and that the distributed double RC circuits are assumed to be in parallel. Also the capacity of each node is assumed to scale with the corresponding node volume (i.e. $Q_i = \frac{Q_{nominal}}{nm}$).

2.5 Thermal Parameterization

As noted earlier in section 2.3, the parameters $K_{inplane}$, $K_{crossplane}$, and $(\rho c)_{battery}$ are unknown. Many papers have cited values for these coefficients [13, 20, 21], but in our case, since each interior node in the jelly roll is considered a lumped node, parameterization was done to quantify the parameters of these lumped nodes. Note that because of the configuration of the setup and its complexity, h is parameterized also and is split into $h_{surface}$ for flow over the RTD sensors and h_{edge} for flow over the edges or sides of the battery. Parameterization was done using least squares method as shown in [12]. The thermal equations were solved using ode solver in MATLAB, and the resulting distributions were interpolated into the sensor locations shown in Fig. 1, and finally a least squares was performed on all 36 sensors for the length of the simulation to find the best fit for the parameters. The objective function J to minimize is:

$$J = \sum_{j=1}^{36} \sqrt{\sum_{i=1}^{t_{end}} (T_{RTD,j,i} - T_{simulated,j,i})^2} \tag{7}$$

where T_{RTD} and $T_{simulated}$ are the measured and simulated temperatures respectively.

Figure 9 shows the current used for parameterization and the corresponding measured temperatures on the surface of the battery. To allow for proper excitation, a 20A, 39A and 50A current amplitudes were used with a pulse width of 20sec each at 50%SOC. Each excitation was 4 hours long to allow for thermal equilibrium.

The values of the parameters that resulted from the thermal parameterization are shown in Tab. 1 along with the thermal parameters of aluminum and air.

Note that $h_{surface} = 6\ W/mK$ and $h_{edge} = 18\ W/mK$ are the convection coefficients from the aluminum casing to the ambient when the fan is turned off (natural convection). The edges of the battery are exposed to the chamber fan which circulates air and maintains the ambient at some specified temperature resulting in higher h_{edge} than $h_{surface}$, while the surfaces are sandwiched in the fixture and have less exposure to circulating air.

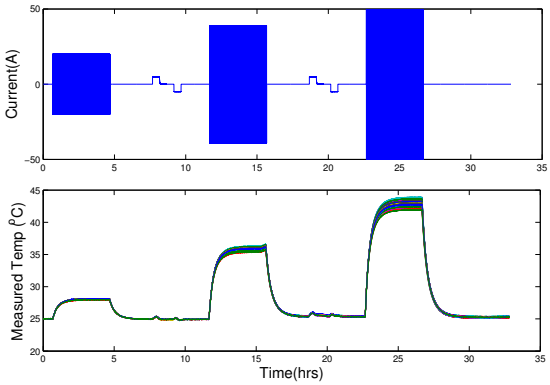

FIGURE 9. CURRENT PROFILE USED FOR THERMAL PARAMETERIZATION AT 25^oC AND THE CORRESPONDING MEASURED SURFACE TEMPERATURES

TABLE 1. IDENTIFIED THERMAL PARAMETERS

Parameter	Jelly roll	Aluminum casing	Air gaps
$K_{inplane}[W/m^2K]$	22	237	0.024
$K_{crossplane}[W/m^2K]$	1.7	237	0.024
$h_{surface}[W/mK]$	—	6	—
$h_{edge}[W/mK]$	—	18	—
$(\rho c)[J/m^3K]$	2.75e6	2.42e6	1200

3 Model Validation

In this section, the proposed model is validated against different experiments that include pulse experiments at different temperatures, states of charge, current amplitude and pulse width. Given that the RTD sensors have an accuracy of 0.5^oC, the model is validated and shows agreement with all experiments both electrically (terminal voltage) and thermally (surface temperature). Table 2 summarizes the list of experiments used for validation and the corresponding root mean square errors (RMSE) on voltage and surface temperature in each case. The first column in Table 2 indicates the type of experiment. The second, third and fourth columns indicate the temperature, SOC and current amplitude at which the experiment was performed. Column 5, which is the pulse profile, has 2 entries which indicate that the first set of pulses have a width of 50 sec, and the second set have 5 sec.

TABLE 2. EXPERIMENTS USED FOR VALIDATION OF COUPLED ELECTRO-THERMAL MODEL

Experiment	Temperature (^oC)	Current Amplitude (A)	SOC (%)	Pulse profile	$V_{RMSE}(mV)$	$T_{max,RMSE}(^oC)$	$T_{min,RMSE}(^oC)$	$T_{mean,RMSE}(^oC)$
Pulse	25	25	50	50/5sec	5.5	0.1	0.2	0.1
Pulse	25	50	50	50/5 sec	7.9	0.3	0.4	0.3
Pulse	25	25	25	50/5 sec	8.6	0.1	0.2	0.1
Pulse	25	25	75	50/5 sec	2.8	0.2	0.2	0.2
Pulse	10	50	50	50/5 sec	8.5	0.4	0.6	0.4
Pulse	-5	50	50	50/5 sec	8.8	1.3	1.8	1.3

3.1 Pulse experiments

In this section, the coupled electro-thermal model is validated against pulsing experiments for varying temperatures, SOCs, current amplitudes and pulse widths. Figure 10 shows the current profile, corresponding SOC, voltage and thermal response, and a spatial temperature distribution profile for both the measured and simulated data at a specified time t. Plots of temperature vs. time show the minimum, maximum and average (simulated and measured) surface temperature evolution. The mean interior temperature is also plotted and it shows that the difference between the mean interior and mean surface temperature is less than 1^oC. The results of pulsing experiments with different conditions are tabulated in Table 2. The results in Table 2 indicate that for higher current rates, the RMSE values are slightly higher than those for lower current rates. This suggests that electrical parameters could be a function of C-rate and could be parameterized accordingly. Moreover, the pulse experiment at -5^oC shows that the RMSE on voltage is 8.8mV which is in good agreement with other results, but the RMSE for the minimum and maximum temperatures exceeds 1^oC. This could suggest that at lower temperatures, the parameterized thermal properties could be different. Finally, looking at the surface spatial temperature distribution shown in Fig. 10, the average and minimum and maximum temperatures seem to be matched, but the overall measured profile is different than the predicted one. Note that, in Fig. 10, the measured spatial temperature is interpolated along the sensor locations and reported only between those locations, while the simulated spatial temperature is reported along the whole surface of the battery. As expected, the simulated profile shows a hotter spot at the center and colder towards the edges, however the measured profiles consistently show that the hot spot is closer to one side (negative terminal) than the other. To investigate this phenomanon, a 50A pulse experiment is repeated with the fan on and fan off. Figure 11 shows the effect of the chamber fan on the spatial temperature distribution. A more defined spatial variation is observed in the case where the fan is on since the circulation of chamber air is asymmetric in cooling one side of the battery more than the other. To mimic this asymmetry, the surface heat transfer coefficient h is increased on the right half of the battery shifting the hot spot as shown in Fig. 12. A more systematic flow tuning will be performed at a later stage by coupling parameterization of this model with a high fidelity model that can solve for flow velocities along with heat transfer.

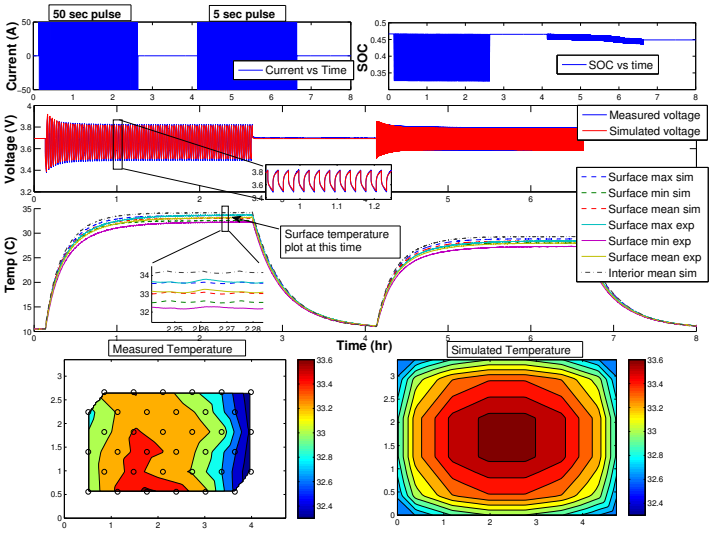

FIGURE 10. PULSE VALIDATION EXPERIMENT AT 10^oC, 50% SOC, AND 50A CURRENT AMPLITUDE

4 Conclusion

An equivalent circuit model has been developed in this paper. The model couples a distributed double RC model network with a 3-D thermal model for a lithium ion pouch cell. The analysis was done on a prismatic NMC lithium ion battery, and the simulated results showed good agreement with experimental data for different experimental conditions. Validation was done for different pulsing profiles (with different ambient temperatures, current amplitudes, pulse widths, and SOCs). The coupling between the electrical and thermal model occurs through local heat

generation and temperature. The different layers of the jelly roll inside the aluminum case of the battery were simplified by assuming an average heat capacity and density, and by introducing anisotropic thermal conductivities ($K_{inplane}$ and $K_{crossplane}$). Electrical parameterization resulted in electrical parameters that are a function of state of charge and temperature, and thermal parameterization resulted in thermal conductivities that are an order of magnitude different. The distributed nodal mesh allowed for validation with thin film RTD sensors mounted across the surface of the cell, while maintaining a fast computational approach similar to that of simple state models. This model has shown agreement with experimental data that replicate pack conditions and was able to capture the average and minimum and maximum temperatures with good accuracy. Future work will include looking at sensor placement issues on the surface of the cell, and reducing and scaling the model to a battery pack to study the spatial temperature variations induced by airflow.

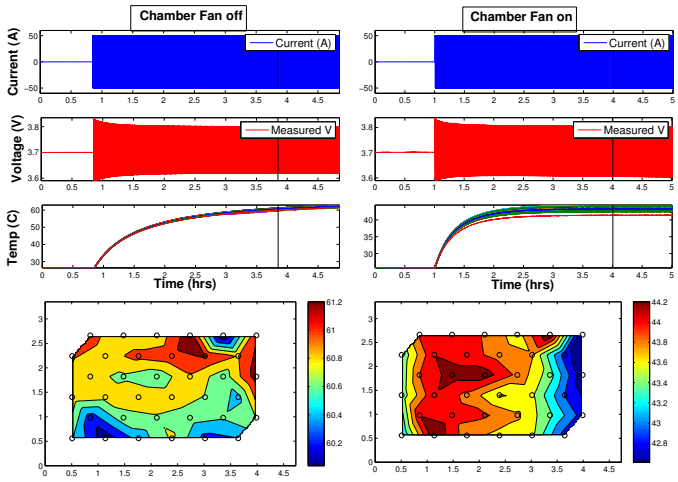

FIGURE 11. EFFECT OF CHAMBER FAN ON SPATIAL TEMPERATURE DISTRIBUTION

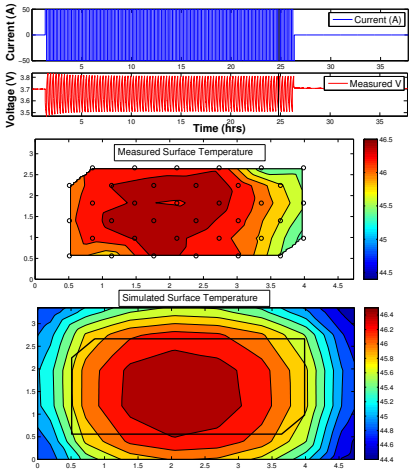

FIGURE 12. INDUCING ASYMMETRY IN SPATIAL TEMPERATURE VARIATION BY INCREASING CONVECTION RATE ON RIGHT HALF PART OF BATTERY

5 Acknowledgment

The information, data, or work presented herein was funded in part by the Advanced Research Projects Agency-Energy (ARPA-E), U.S. Department of Energy, under Award Number DE-AR0000269. The authors would like to acknowledge the contribution of Aaron Knobloch and Christopher Kapusta from GE Global Research and Brian Engle from Amphenol Advanced Sensors for providing the RTD sensors and for their continuous feedback and support.

6 Disclaimer

The information, data, or work presented herein was funded in part by an agency of the United States Government. Neither the United States Government nor any agency thereof, nor any of their employees, makes any warranty, express or implied, or assumes any legal liability or responsibility for the accuracy, completeness, or usefulness of any information, apparatus, product, or process disclosed, or represents that its use would not infringe privately owned rights. Reference herein to any specific commercial product, process, or service by trade name, trademark, manufacturer, or otherwise does not necessarily constitute or imply its endorsement, recommendation, or favoring by the United States Government or any agency thereof. The views and opinions of authors expressed herein do not necessarily state or reflect those of the United States Government or any agency thereof.

REFERENCES

[1] Mandal, B. K., Padhi, A. K., Shi, Z., Chakraborty, S., and Filler, R., 2006. "Thermal runaway inhibitors for lithium battery electrolytes". *Journal of Power Sources,* **161**(2), pp. 1341 – 1345.

[2] Bernardi, D., Pawlikowski, E., and Newman, J., 1985. "A general energy balance for battery systems". *Journal of The Electrochemical Society,* **132**.

[3] Doyle, M., Fuller, T. F., and Newman, J., 1993. "Modeling of galvanostatic charge and discharge of the lithium/polymer/insertion cell". *Journal of the Electrochemical Society,* **140**.

[4] Fuller, T. F., Doyle, M., and Newman, J., 1994. "Simulation and optimization of the dual lithium ion insertion cell".

Journal of the Electrochemical Society, **1**.

[5] Safari, M., Morcrette, M., Teyssot, A., and Delacourta, C., 2009. "Multimodal physics-based aging model for life prediction of li-ion batteries". *Journal of the Electrochemical Society,* **156**.

[6] Lin, X., Perez, H. E., Siegel, J. B., Stefanopoulou, A. G., Li, Y., Anderson, R. D., Ding, Y., and Castanier, M. P., 2013. "Online parameterization of lumped thermal dynamics in cylindrical lithium ion batteries for core temperature estimation and health monitoring". *IEEE Transactions on Control System Technology, Accepted pending minor revisions*.

[7] Murashko, K., Pyrhonen, J., and Laurila, L., 2013. "Three-dimensional thermal model of a lithium ion battery for hybrid mobile working machines: Determination of the model parameters in a pouch cell". *Energy Conversion, IEEE Transactions on,* **28**(2), pp. 335–343.

[8] Einhorn, M., Conte, F., Kral, C., and Fleig, J., 2013. "Comparison, selection, and parameterization of electrical battery models for automotive applications". *Power Electronics, IEEE Transactions on,* **28**(3), pp. 1429–1437.

[9] Hu, Y., Yurkovich, S., Guezennec, Y., and Yurkovich, B., 2011. "Electro-thermal battery model identification for automotive applications". *Journal of Power Sources,* **196**(1), pp. 449 – 457.

[10] Lam, L., Bauer, P., and Kelder, E., 2011. "A practical circuit-based model for li-ion battery cells in electric vehicle applications". In Telecommunications Energy Conference (INTELEC), 2011 IEEE 33rd International, pp. 1–9.

[11] Gao, L., Liu, S., and Dougal, R., 2002. "Dynamic lithium-ion battery model for system simulation". *Components and Packaging Technologies, IEEE Transactions on,* **25**(3), Sep, pp. 495–505.

[12] Perez, H. E., Siegel, J. B., Lin, X., Ding, Y., and Castanier, M. P., 2012. "Parameterization and validation of an integrated electro-thermal lfp battery model". In 2012 ASME Dynamic Systems Control Conference, Oct 2012.

[13] Jung, S., and Kang, D., 2014. "Multi-dimensional modeling of large-scale lithium-ion batteries". *Journal of Power Sources,* **248**(0), pp. 498 – 509.

[14] Smith, K., Kim, G.-H., Darcy, E., and Pesaran, A., 2010. "Thermal/electrical modeling for abuse-tolerant design of lithium ion modules". *International Journal of Energy Research,* **34**, pp. 204–215.

[15] Fleckenstein, M., Bohlen, O., Roscher, M. A., and Bker, B., 2011. "Current density and state of charge inhomogeneities in li-ion battery cells with lifepo4 as cathode material due to temperature gradients". *Journal of Power Sources,* **196**(10), pp. 4769 – 4778.

[16] Chen, S., Wan, C., and Wang, Y., 2005. "Thermal analysis of lithium-ion batteries". *Journal of Power Sources,* **140**(1), pp. 111 – 124.

[17] Inui, Y., Kobayashi, Y., Watanabe, Y., Watase, Y., and Kitamura, Y., 2007. "Simulation of temperature distribution in cylindrical and prismatic lithium ion secondary batteries". *Energy Conversion and Management,* **48**(7), pp. 2103 – 2109.

[18] Samba, A., Omar, N., Gualous, H., Firouz, Y., den Bossche, P. V., Mierlo, J. V., and Boubekeur, T. I., 2014. "Development of an advanced two-dimensional thermal model for large size lithium-ion pouch cells". *Electrochimica Acta,* **117**(0), pp. 246 – 254.

[19] Gerver, R. E., and Meyers, J. P., 2011. "Three-dimensional modeling of electrochemical performance and heat generation of lithium-ion batteries in tabbed planar configurations". *Journal of The Electrochemical Society,* **158**, pp. A835 – A843.

[20] Taheri, P., and Bahrami, M., 2012. "Temperature rise in prismatic polymer lithium-ion batteries: An analytic approach". *SAE International,* **5**.

[21] Maleki, H., Hallaj, S. A., Selman, J. R., Dinwiddie, R. B., and Wang, H., 1999. "Thermal properties of lithium-ion battery and components". *Journal of The Electrochemical Society,* **146**, pp. 947–954.

[22] Hallaj, S. A., Prakash, J., and Selman, J., 2000. "Characterization of commercial li-ion batteries using electrochemical-calorimetric measurements". *Journal of Power Sources,* **87**, pp. 186 – 194.